

Quantitative mapping of zinc fluxes in the mammalian egg reveals the origin of fertilization-induced zinc sparks

Emily L. Que¹, Reiner Bleher^{1,2}, Francesca E. Duncan³, Betty Y. Kong³, Sophie C. Gleber⁴, Stefan Vogt⁴, Si Chen⁴, Seth A. Garwin^{1,5}, Amanda R. Bayer^{1,5}, Vinayak P. Dravid^{2,5,6}, Teresa K. Woodruff^{1,3,7*} and Thomas V. O'Halloran^{1,5,7*}

Fertilization of a mammalian egg initiates a series of 'zinc sparks' that are necessary to induce the egg-to-embryo transition. Despite the importance of these zinc-efflux events little is known about their origin. To understand the molecular mechanism of the zinc spark we combined four physical approaches that resolve zinc distributions in single cells: a chemical probe for dynamic live-cell fluorescence imaging and a combination of scanning transmission electron microscopy with energy-dispersive spectroscopy, X-ray fluorescence microscopy and three-dimensional elemental tomography for high-resolution elemental mapping. We show that the zinc spark arises from a system of thousands of zinc-loaded vesicles, each of which contains, on average, 10^6 zinc atoms. These vesicles undergo dynamic movement during oocyte maturation and exocytosis at the time of fertilization. The discovery of these vesicles and the demonstration that zinc sparks originate from them provides a quantitative framework for understanding how zinc fluxes regulate cellular processes.

The Zn^{2+} ion is well known as an important metalloprotein cofactor that is tightly regulated by cells^{1–4}. Unlike other essential divalent metal ions such as Mg^{2+} and Ca^{2+} , Zn^{2+} is typically bound with a high affinity (that is, $K_D < 10^{-12}$) in the catalytic active site of metalloenzymes or in catalytically inactive sites of proteins involved in regulation, transcription and translation. Recently, extraordinary cell-driven changes in the total intracellular Zn^{2+} content have been identified as key events regulating the cell cycle in the mammalian egg: zinc influx is essential during maturation in the 16 hours before fertilization and zinc efflux is essential for embryo formation in the two hours following fertilization^{5–12}. These studies reveal that zinc fluctuations serve an instructive or regulatory role in controlling cell-cycle progression at the earliest stage of embryonic development. Our goal is to understand the molecular mechanisms of how cells use zinc fluxes to make major decisions.

The female reproductive cells in the mouse have many advantageous properties for probing how cells use inorganic chemistry to control decision-making processes. Immature mouse oocytes are readily isolated and the entire process of their maturation into an egg and the subsequent conversion into an embryo on fertilization by a sperm cell all transpires under 24 hours. Three key intermediary stages are well known and progression is controlled by biological checkpoints. Female reproductive cells found within the ovary are arrested in the prophase of meiosis I and are called germinal vesicle (GV) oocytes. During meiotic maturation, the GV oocyte exits from prophase I arrest and progresses for 12–16 hours until it stops and arrests in the metaphase of meiosis II, at which point the

reproductive cell is called an MII egg: this is the first point at which it is competent for fertilization. In the process of maturation, we have shown that the mouse oocyte accrues 20 billion zinc atoms, which corresponds to a >50% increase in total cellular zinc content, in a time span of several hours⁵. This increase is essential: if zinc accrual is abrogated *in vitro* using a zinc chelator or *in vivo* by acute dietary zinc deficiency, then progression to MII and fertilization are significantly impaired^{5,8,11,13}. In contrast, fertilization or activation of the MII egg is accompanied by a decrease in the total zinc content of about 10 billion zinc atoms⁵, as quantified by X-ray fluorescence microscopy (XFM). The loss of zinc at the end of meiosis is necessary to mediate the egg-to-embryo transition as an artificial maintenance of high intracellular zinc prevents pronuclear formation⁸. Moreover, the treatment of mature eggs with an intracellular zinc chelator leads to a high rate of parthenogenetic activation, or egg activation, in the absence of sperm^{6,10}. In parthenogenetic activation, the early cell-division stages of embryogenesis can occur for several days, but a viable embryo does not result. It is not known how these essential fluxes in zinc concentration are controlled at the cellular and molecular levels. Recent studies reveal a plausible path for the uptake of zinc during maturation of the GV oocyte into the MII egg. During maturation, we have identified two abundant zinc transporters in the outer or ooplasmic membrane, namely ZIP6 and ZIP10. These proteins mediate zinc influx during the oocyte-to-egg transition¹⁴.

In contrast to the uptake in zinc that occurs during maturation, fertilization triggers a series of repetitive efflux events known as 'zinc sparks' that release zinc into the extracellular space⁶. Zinc flux

¹The Chemistry of Life Processes Institute, Northwestern University, Evanston, Illinois 60208, USA. ²Northwestern University Atomic and Nanoscale Characterization Experimental Center, Evanston, Illinois 60208, USA. ³Department of Obstetrics and Gynecology, Northwestern University, Feinberg School of Medicine, Chicago, Illinois 60611, USA. ⁴X-ray Science Division, Argonne National Laboratory, Argonne, Illinois 60439, USA. ⁵Department of Chemistry, Northwestern University, Evanston, Illinois 60208, USA. ⁶Department of Materials Science and Engineering, Northwestern University, Evanston, Illinois 60208, USA. ⁷Department of Molecular Biosciences, Northwestern University, Evanston, Illinois 60208, USA. *e-mail: t-ohalloran@northwestern.edu; tkw@northwestern.edu

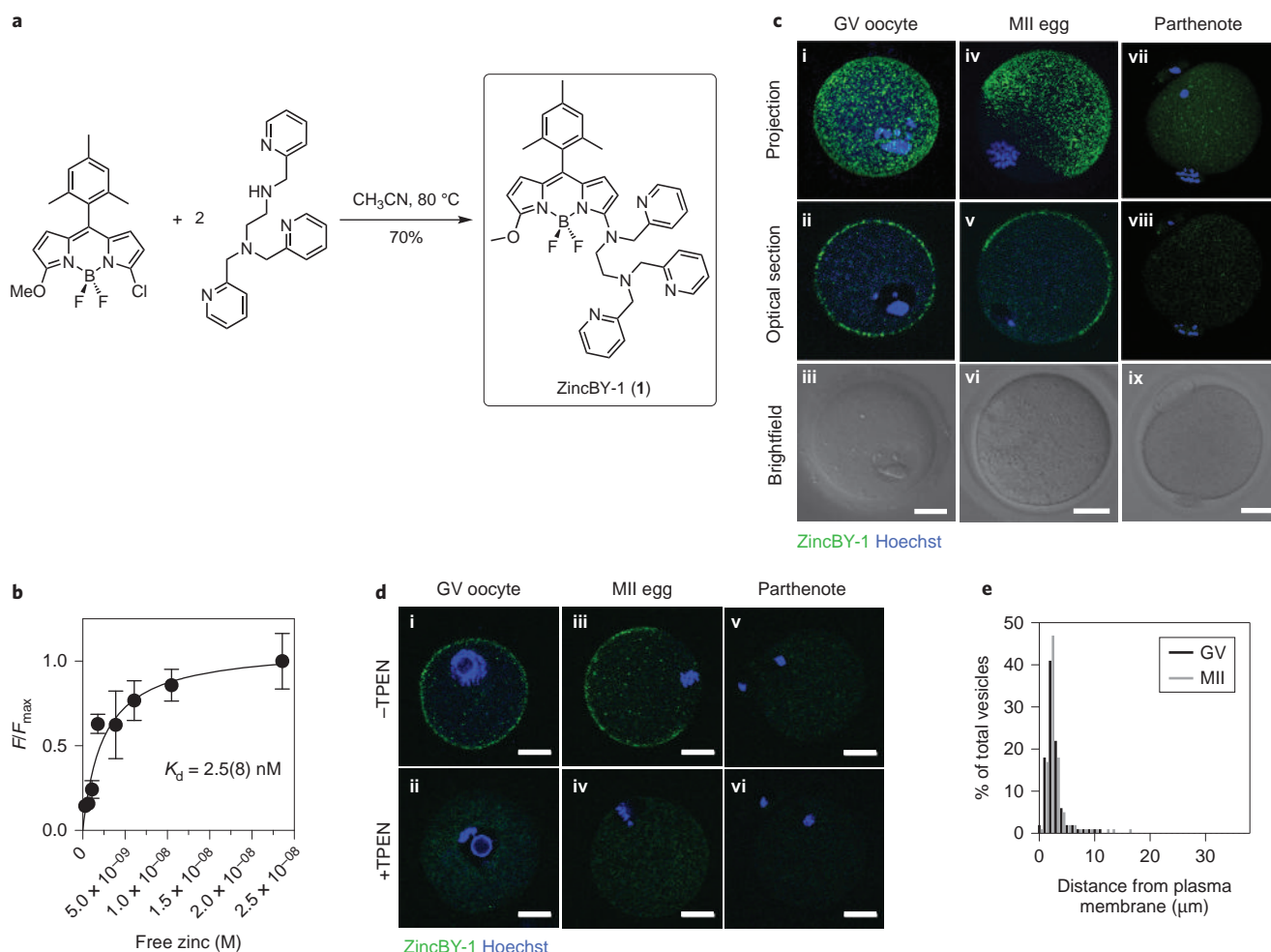


Figure 1 | Vital zinc probe reveals cortical compartments in the female gamete in mouse. **a**, Final step (see Methods) in the synthesis of ZincBY-1, a novel fluorescent zinc probe. **b**, Fluorescence emission of ZincBY-1 in EGTA-buffered Zn²⁺ solutions. Error bars represent \pm s.e.m. Spectra were acquired in 100 mM KNO₃, 50 mM HEPES, pH 7.2, $\lambda_{\text{ex}} = 520$ nm. Integrated emission (530–700 nm) was plotted versus calculated $[\text{Zn}_{\text{free}}^{2+}]$ and fitted to the apparent $K_d = 2.5$ nM. **c**, GV oocyte, MII egg and parthenote incubated with 50 nM ZincBY-1 (green) and DNA probe Hoechst 33342 (blue). Representative z-stack projection (i, iv and vii), confocal optical slice (ii, v and viii) and brightfield (iii, vi and ix) images are shown. Bright, punctate cortical fluorescence from ZincBY-1 is observed in GV and MII cells. **d**, Incubation with 10 μM TPEN for ten minutes abolished the cortical fluorescence in ZincBY-1 stained cells. **e**, Distance of ZincBY-1 compartments from the PM in GV (black) and MII (grey) cells. Vesicle positions were sorted into 1 μm bins and plotted as a histogram; >90% of compartments were within 5 μm of the membrane in both cell types. Scale bars in **c** and **d**, 20 μm .

during fertilization could involve ion channels, the secretory pathway or other cellular mechanisms, but a model has not been identified unequivocally. Treatment with parthenogenetic activation agents also induces zinc sparks⁶. Zinc sparks are observed at the cell periphery in a manner that resembles the distribution of zinc in the MII-arrested egg⁶. Based on these observations, we hypothesized that zinc sparks originate from the release of discrete cortical zinc-containing compartments. Other models for the zinc spark are not ruled out by current published results. There are a number of general pathways by which zinc might move from the cytosol into the extracellular space during a zinc-spark event. For instance, unidentified orthologues of voltage- and ligand-gated ion channels, ATPase7 family of copper transporters or other integral membrane proteins, including members of the ZnT family of zinc and iron transporters, could conceivably facilitate/permit the movement of Zn²⁺ ions^{15–17}.

Our ability to distinguish between these models is compromised by the paucity of quantitative physical methods with sufficiently high spatial resolution, with specificity for specific metal ions and with enough sensitivity to establish metal concentrations in subcellular compartments. As a consequence, zinc has not been

monitored throughout an entire biological process in a manner that allows for a mass-balance analysis of zinc flux in an individual cell, despite the strong evidence that dynamic changes in zinc can regulate key biological decisions. To better address these models for the zinc spark, we developed new chemical tools and applied cutting-edge elemental imaging in single cells to determine quantitatively local changes in the cellular zinc quota before and during fertilization of the mammalian egg. These approaches include the synthesis of a novel zinc-specific probe that can be used at nanomolar concentrations for live-cell imaging, scanning transmission electron microscopy with energy-dispersive spectroscopy (STEM-EDS) to map biological zinc directly at the ultrastructural level, X-ray fluorescence nanoprobe microscopy to quantify zinc within compartments and three-dimensional (3D) X-ray fluorescence tomography to establish the total zinc distribution within the cell. Using these methods together, for the first time we established that the zinc spark originates from thousands of cortically enriched, zinc-loaded secretory compartments. These vesicles contain ~15% of the total zinc content of the egg and are released from the egg following activation. This vesicular zinc release accounts for the precise loss observed during zinc sparks. Intense interest in putative

zinc secretory systems (including those in neurons, pancreatic beta islets and immune cells)^{18–22} has largely utilized qualitative methods to characterize the zinc flux. This work provides an unprecedented quantitative demonstration of regulatory fluxes in transition-metal content at the single-cell level and firmly establishes zinc-dependent pathways in the meiotic cell-cycle regulation in the mammalian egg.

Results

Characterization of the zinc sensor ZincBY-1. Vital fluorogenic zinc sensors facilitate the detection of changes in labile zinc concentration in biological samples^{23–27}. We developed a new zinc sensor, ZincBY-1 (1, Fig. 1a), with nanomolar affinity for labile zinc (Fig. 1b). Compared with the commercially available zinc sensor FluoZin-3-AM, which requires sensor concentrations up to 10 μM for visualization⁶, ZincBY-1 can be used to highlight zinc in the egg at treatment concentrations as low as 50 nM (Fig. 1c), a 200-fold lower concentration than that for FluoZin-3-AM. In addition, ZincBY-1 does not require AM-ester moieties for cell membrane permeability. As a result, potentially toxic cleavage products of AM-esters (formaldehyde and acetic acid)²⁸ are not introduced to the cell when ZincBY-1 is utilized.

ZincBY-1 is synthesized from an asymmetric BODIPY (boron dipyrromethene) core^{29,30} and a polypyridine zinc chelator³¹ (Fig. 1a). The zinc-loaded probe has a modest quantum yield (Supplementary Table 1), and in aqueous buffer 50 nM ZincBY-1 exhibits a 4.6-fold increase in fluorescence brightness in the presence of zinc ($\lambda_{\text{ex}} = 520 \text{ nm}$, $\lambda_{\text{em}} = 543 \text{ nm}$) (Supplementary Fig. 1 and Supplementary Table 1). ZincBY-1 displays an apparent zinc dissociation constant (K_{d}) of $2.5 \pm 0.8 \text{ nM}$ (Fig. 1b), as determined using EGTA (ethylene glycol-bis(2-aminoethylether)-*N,N,N',N'*-tetraacetic acid) as a competing ligand for zinc (see the Supplementary Methods). The fluorescence response is selective for Zn^{2+} over a range of biologically essential metal ions, including Ca^{2+} , Mg^{2+} , K^{+} and Na^{+} . The addition of copper ions induces quenching of ZincBY-1 and inhibits the zinc response. This is not surprising, as pyridine-based ligands have previously been shown to have an appreciable affinity towards both Cu^{2+} and Cu^{+} (ref. 32). However, this feature of the probe should not affect the utility of this reagent in the egg because copper is an order of magnitude lower in concentration than zinc⁵ and the majority of copper ions are likely to be tightly bound to metalloproteins³³. The heavy-metal ions Hg^{2+} and Cd^{2+} also induce a ZincBY-1 fluorescence increase; however, these are not abundant in normal egg cells⁵. Finally, the fluorescence of both apo and zinc-bound ZincBY-1 is not affected by pH changes within the physiologically relevant range (pH 4–8.5) (Supplementary Fig. 1 and Supplementary Table 1).

In addition to eggs (Fig. 1c, described in further detail below), ZincBY-1 can also monitor zinc stores in other cell types, including mouse spermatozoa, a cell known to contain spatially localized zinc^{34–36}. Specifically, silver staining after autometallography of fixed sperm identified zinc enrichment within the acrosome³⁵. We therefore imaged live sperm with ZincBY-1 as a positive control. Discrete fluorescence was located in the expected acrosomal region of sperm incubated with 50 nM ZincBY-1. Moreover, the fluorescence was quenched after incubation with TPEN (*N,N,N',N'*-tetrakis(2-pyridylmethyl)ethylenediamine) (Supplementary Fig. 2). This same localization is similarly observed when live sperm are imaged with micromolar amounts of the zinc probes FluoZin-3-AM (Supplementary Fig. 2) and TSQ (*N*-(6-methoxy-8-quinolyl-*p*-toluenesulfonamide), as found in an experiment performed in hamster sperm³⁴.

Spatiotemporal dynamics of labile zinc compartments during meiotic maturation. Oocytes and eggs incubated with 50 nM ZincBY-1 have discrete punctate fluorescent structures that changed subcellular localization as a function of meiotic stage. GV oocytes

displayed uniformly distributed punctate structures throughout the cell cortex (Fig. 1c,i,ii). MII eggs had a similar staining pattern; however, the distribution was concentrated predominantly in the vegetal hemisphere of the cell, opposite the region where metaphase chromosomes localize (Fig. 1c,iv,v). Strikingly, the distribution of labile zinc changed from symmetrical to polarized between the GV to MII stages, which mirrors the changes in total zinc distribution previously observed by XFM⁶.

To assess the biological specificity of ZincBY-1, we performed several controls. First, ZincBY-1 fluorescence was abolished by treatment with the heavy-metal chelator TPEN³⁷ (Fig. 1d), which indicates that the signal is caused by probe interaction with labile zinc. In addition, punctate peripheral fluorescence was still observed following the centrifugation of ZincBY-1 solutions prior to incubation (20 minutes, 3,750 revolutions per minute), which demonstrates that the observed punctate fluorescence is probably not caused by the cellular uptake of nanoscale aggregates³⁸ (data not shown). In addition, using dynamic light scattering we did not observe aggregates at ZincBY-1 concentrations below 500 nM (Supplementary Table 2); however, we are unable to exclude the possibility that aggregates cannot be detected at these low concentrations. The ZincBY-1 staining pattern in eggs is consistent with that obtained using higher concentrations of other intracellular zinc probes, including FluoZin-3-AM³⁹ and Zinpyr-4⁴⁰. Both of these probes display hemispherical, punctate cortical fluorescence patterns in the MII egg at concentrations of 5–10 μM (Supplementary Fig. 3; see also Kim *et al.*⁶). However, neither probe provided a signal when the eggs were treated at a 50 nM concentration.

Quantitative analysis of the staining revealed that GV oocytes contained significantly more zinc-rich compartments than MII eggs ($9,000 \pm 200$ ($N = 36$) versus $8,000 \pm 300$ ($N = 30$), $P = 0.0021$). More than ~90% of zinc-enriched compartments are localized within 5 μm of the plasma membrane (PM) in both cell types (Fig. 1e). The small decrease in the number of zinc-enriched compartments associated with meiotic maturation suggests that compartments are lost in addition to being reorganized during meiotic maturation. Although the majority of observed compartments are localized to the egg cortex, small numbers of vesicles are observed throughout the egg, which indicates that ZincBY-1 is able to penetrate into the cell (Supplementary Fig. 4). In addition, MII eggs incubated with zinc pyrithione before and after exposure to ZincBY-1 revealed that this fluorescent probe penetrates beyond the cortical region and distributes throughout the egg (Supplementary Fig. 5). Although ZincBY-1 fluorescence can be observed throughout the cell, the majority of the signal is observed in intracellular compartments. TPEN controls (Fig. 1d) support the zinc dependence of this localized fluorescence.

The punctate nature of ZincBY-1 staining is consistent with the presence of discrete vesicular compartments that contain high levels of labile zinc; however, the cellular components associated with these structures are unknown. We investigated whether zinc transporters displayed a similar localization as these could be used to facilitate zinc movement into and out of the vesicles. Immunofluorescence experiments on fixed GV and MII oocytes with antibodies to ZIP6, ZIP10 and ZnT3²⁰ revealed a cortical staining pattern at the PM for ZIP6 and ZIP10 but not for ZnT3 (data not shown, ZIP6 and ZIP10 data were recently published in Kong *et al.*¹⁴). The localization and relative number of ZincBY-1-stained compartments at the GV and MII stages are strikingly similar to a known vesicular cohort in eggs, that is, the cortical granules (CGs). CGs are Golgi-derived vesicles distributed throughout the oocyte cortex during oogenesis^{41,42}. CG exocytosis occurs at the time of fertilization and results in the release of enzymes that modify the zona pellucida (ZP) and aid in the block to polyspermy^{43,44}. To compare the distribution of the zinc-enriched structures to that of CGs, cells were fixed and stained for CGs

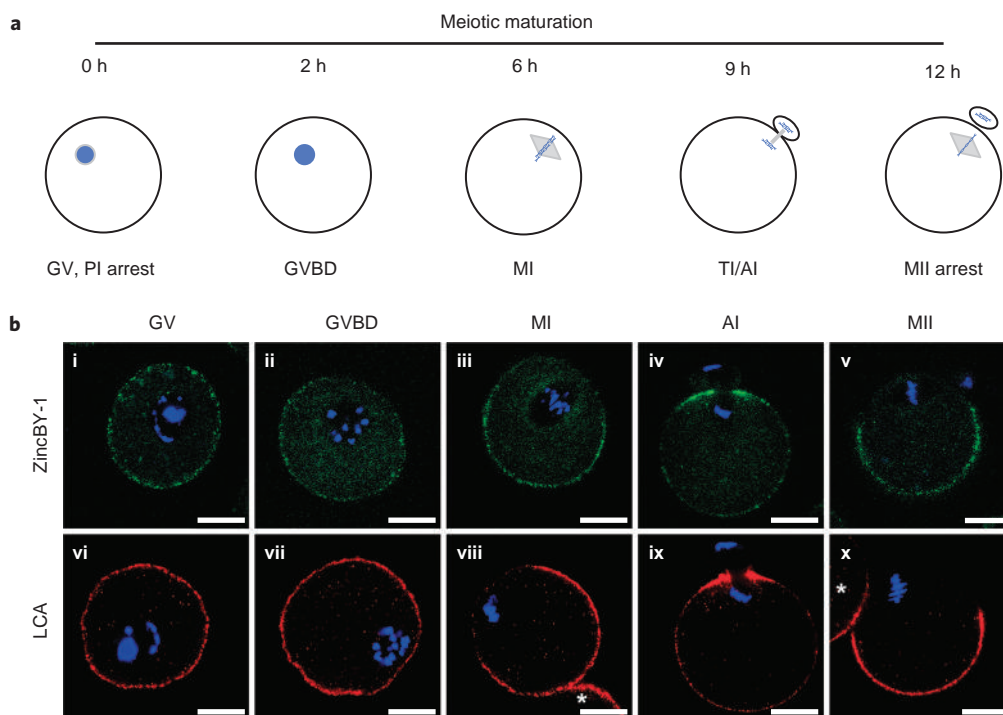


Figure 2 | Labile zinc is cortically localized in the oocyte and tracks with CG staining. **a**, Schematic of meiotic maturation. GV oocytes in the ovary are arrested at prophase I (PI) of meiosis. Upon hormonal signalling, maturation begins and the cell progresses through meiosis until it arrests at MII, at which point the egg is competent for fertilization. Intervening stages during maturation include germinal vesicle breakdown (GVBD), metaphase I (MI) and telophase I/anaphase I (TI/AI). **b** (i–v) Samples at GV (i), GVBD (ii), MI (iii), AI (iv) and MII (v) were labelled with the zinc-specific probe ZincBY-1 (50 nM, green) to track labile zinc, and counterstained with Hoechst 33342 to label DNA (blue). vi–x, Following zinc imaging, cells were fixed and stained for CGs using fluorescently labelled *Lens culinaris* agglutinin (LCA, red) and counterstained for DNA with DAPI (blue). Staining patterns for zinc and LCA are similar at each stage of maturation, which suggests that zinc-enriched structures may represent the same vesicles as, or comprise a subpopulation of, the CGs. Representative optical confocal sections for each meiotic stage are shown. At least five oocytes were visualized at each stage in three independent experiments. Scale bars, 25 μm . *Adjacent oocyte.

after live-cell labile-zinc imaging at various stages during meiotic maturation (Fig. 2). As the detection of labile zinc requires live-cell imaging and the detection of CGs requires fixation, we could not investigate their colocalization simultaneously in the same cell. Nevertheless, a sequential staining procedure demonstrated that the distribution of labile zinc (Fig. 2b,i–v) was similar to the CG distribution (Fig. 2b,vi–x). This colocalization was particularly striking at anaphase I, when both labile zinc and CGs were concentrated at the region between the oocyte and polar body. These data suggest that the zinc-enriched structures may be the same vesicles as, or comprise a subpopulation of, the CGs.

Ultrastructural elemental mapping corroborates the presence of cortical zinc-rich vesicular structures. To further examine whether ZincBY-1-labelled sites were, in fact, zinc-rich vesicles, we developed, optimized and used a suite of elemental mapping approaches for the direct detection of zinc in subcellular compartments, STEM-EDS, Bionanoprobe XFM and XFM tomography. With STEM-EDS, images of high spatial resolution (<10 nm) can be acquired that provide information about cellular structure and elemental content; however, highly accurate concentrations are difficult to establish using this technique. Bionanoprobe XFM complements STEM-EDS by enabling acquisition of images with good spatial resolution (<100 nm) and quantitative information about elemental content. Cellular structures, however, cannot be visualized precisely. XFM tomography allows us to explore further the zinc distribution in these large cells by providing 3D elemental information.

Traditional elemental mapping approaches require the use of sample fixation and embedding, which is known to lead to metal-

ion loss⁴⁵. Thus, we developed a new technique for detecting zinc in fixed samples based on the first step of the Timm silver-staining method (autometallography)^{46,47}. In traditional Timm staining, biological samples are treated with a sulfide source to precipitate out highly insoluble metal sulfides, including ZnS (K_{sp} (sp, solubility product) = $4 \times 10^{-26} \text{ M}^2$)⁴⁸, and precipitation is followed by silver enhancement. The resulting electron-dense silver granules provide an indirect indication of pools of zinc ions (see the Supplementary Information and Supplementary Fig. 6). However, the size of the granules is a function of silver-reduction conditions and does not accurately reflect the size of the biological compartment. To address these possible artefacts we eliminated the silver-enhancement step and optimized the protocol of hydrogen-sulfide treatment for egg analysis. Briefly, whole freshly fixed cells were treated with 20 mM hydrogen sulfide/bisulfide solutions at a neutral pH under conditions that stabilize Zn^{2+} ions in the form of ZnS; these samples could then be processed for elemental mapping (Fig. 3a).

Although sulfide treatment will not precipitate sulfides of more-abundant cellular metals, such as calcium (K_{sp} (CaS) = $8 \times 10^{-7} \text{ M}^2$), it can fix any weakly bound copper (K_{sp} (CuS) = $5 \times 10^{-41} \text{ M}^2$, K_{sp} (Cu₂S) = $4 \times 10^{-53} \text{ M}^3$) or iron stores (K_{sp} (FeS) = $1 \times 10^{-21} \text{ M}^2$)⁴⁸. To resolve directly the identity of the metal, we determined the spatially resolved X-ray fluorescence spectroscopic signatures of individual sulfide-fixed compartments using two distinct approaches, STEM-EDS and XFM using a high-resolution nanoprobe.

First, the elemental content of individual compartments in MII eggs was determined at the ultrastructural level using a scanning transmission electron microscope designed with enhanced dual detectors for EDS (Fig. 3b). The dual EDS detector design provides

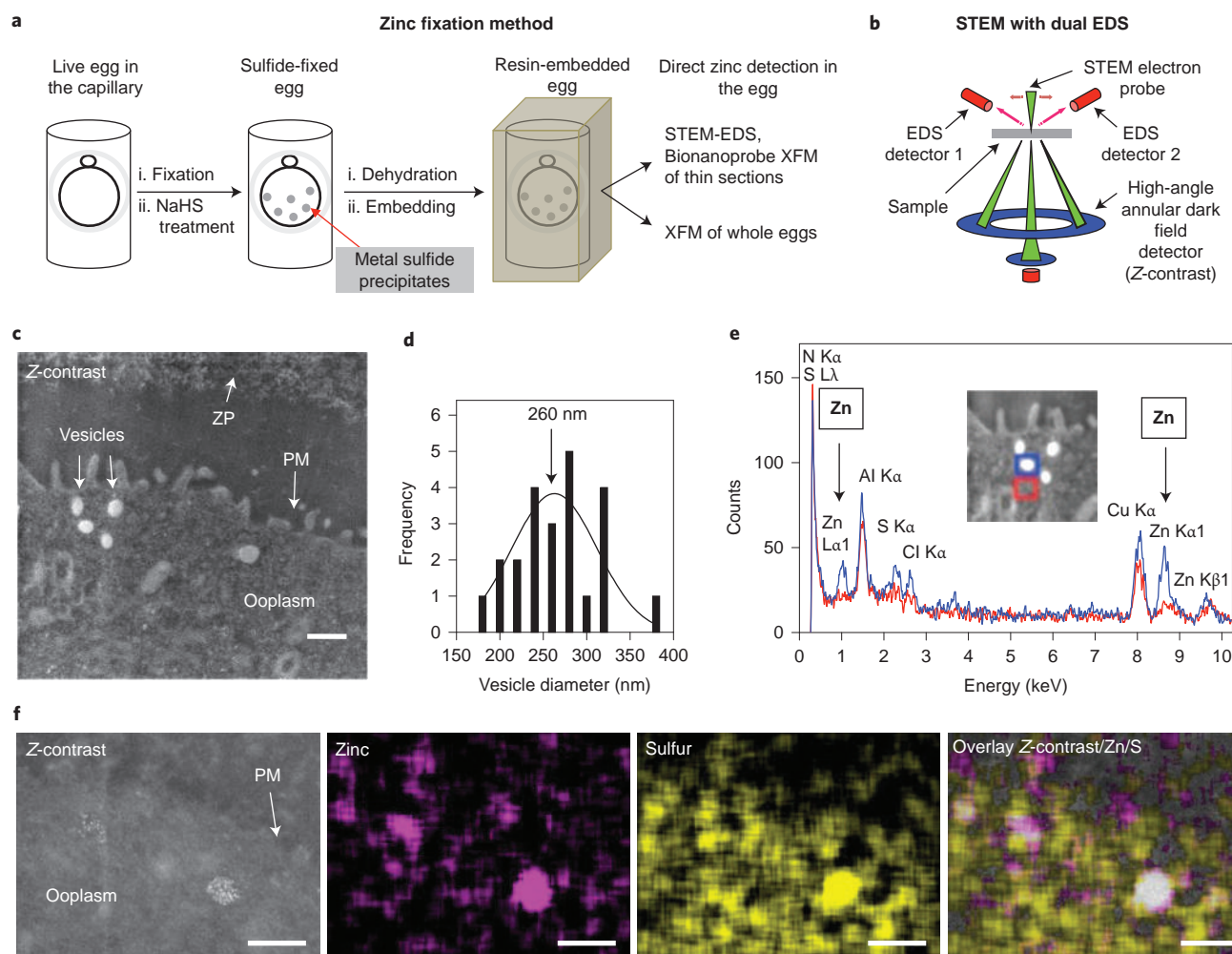


Figure 3 | Zinc fixation enables ultrastructural identification of zinc-enriched cortical compartments by STEM-EDS. **a**, Zinc-fixation schematic. Eggs were fixed and treated with NaHS to form ZnS. Following ethanol dehydration and resin embedding, eggs were used intact for XFM tomography or sectioned prior to STEM-EDS or XFM Bionanoprobe analysis. **b**, Diagram of STEM microscope with dual EDS detectors for zinc mapping⁴⁹. **c**, Z-contrast image of a 200 nm section of a resin-embedded MII egg following zinc fixation. Vesicles, ZP, PM and ooplasm are indicated. The bright and dark areas indicate regions with high and low molecular weight content, respectively. The bright signal is concentrated in cortical compartments. Scale bar, 0.5 μm . **d**, Histogram of the diameters of cortical compartments in STEM-EDS samples (20 nm bins). The distribution centres on a diameter of ~ 260 nm. Data are from 23 zinc-enriched compartments from eight eggs. **e**, EDS spectra of the bright compartment (blue) and cytoplasm (red) in the inset. The zinc signal is enriched in the compartment relative to the cytoplasm. **f**, Z-contrast, zinc and sulfur EDS maps of a cortical region in an MII egg. The overlay demonstrates that zinc-rich regions correspond to areas high in sulfur and in electron density (Z-contrast). Scale bars, 500 nm.

a nominal collection angle of 0.76 steradians, and thus records peak intensities that are much higher than those of conventional single-detector systems⁴⁹. The multimodal capabilities of this instrument allow both anatomical and elemental imaging of samples, which allows us to push the boundaries of bioelemental imaging. Thin sections (200 nm) of a sulfide-fixed, resin-embedded MII egg were prepared, imaged and analysed by STEM for cellular structure and elemental content. Bright, vesicular structures near the ooplasmic membrane are evident in the Z-contrast image (Fig. 3c and Supplementary Fig. 7), indicative of elements with high molecular weights in these regions. They range from 180 to 375 nm in diameter (*d*) with the average $d = 260 \pm 50$ nm ($n = 23$, Fig. 3d). EDS spectra measured in electron-dense regions and nearby cytoplasm revealed a significant zinc-signal intensity above background in the electron-dense regions (Fig. 3e). Elemental map analysis of raster scans of an egg section (Fig. 3f) further indicated that zinc fixation gives tight zinc distributions that overlay with electron-dense regions in the Z-contrast image. Furthermore, analysis of zinc-enriched structures revealed a zinc to sulfur mole ratio of ~ 1 ,

consistent with the formation of nanocrystalline deposits of ZnS as the major metal-sulfide species within distinct boundaries (Supplementary Fig. 8). This approach provides the first ultrastructural maps of zinc in cells at <10 nm resolution. The size, morphology, chemistry and physiology support the designation of these compartments as zinc-enriched cortical vesicles.

X-ray fluorescence bionanoprobe microscopy allows the quantification of zinc in cortical compartments. To test further the conclusions from ultrastructural mapping and to address the quantity of zinc in each structure, we used a synchrotron-based X-ray fluorescence microscope bionanoprobe designed for the quantitative high-resolution elemental mapping of biological samples⁵⁰. High-resolution XFM zinc maps of thin sections of sulfide-treated MII eggs also showed a dense array of zinc-enriched compartments at the cell cortex, consistent with the live-cell fluorescence and STEM-EDS results (Fig. 4a). The iron and copper are not enriched near the PM. Quantification of zinc content in these regions allows for the determination of

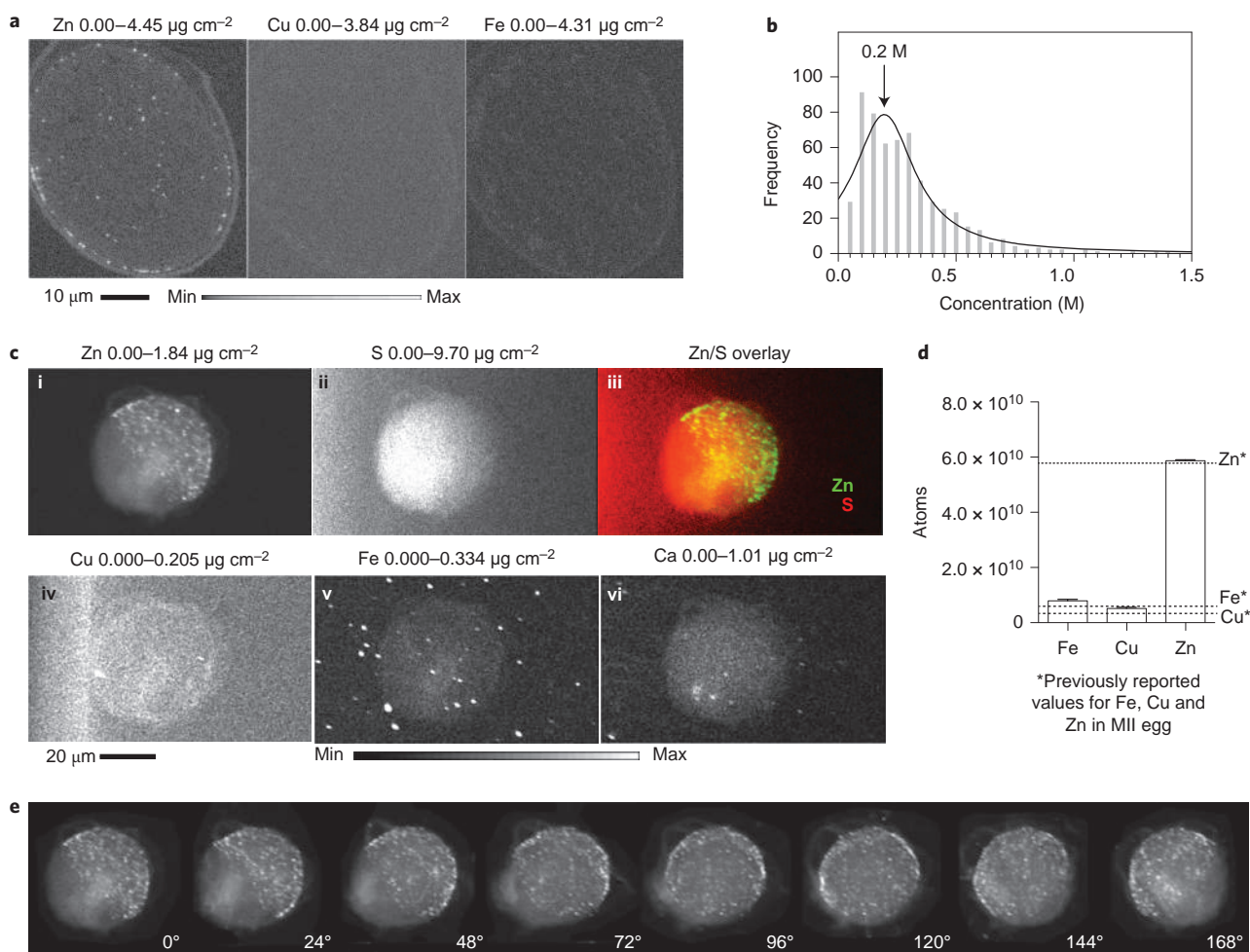


Figure 4 | XFM and tomography provide zinc quantification and mapping within the egg. **a**, Bionanoprobe XFM images of a 400 nm thick egg section. The zinc, copper and iron maps are shown with concentration ranges. Pixels, $100 \times 100 \text{ nm}^2$. A high [Zn] is observed in the punctate cortical structures. **b**, Histogram of [Zn] in punctate regions (bins = 0.05 M). Data were fitted to a Lorentzian distribution (black line) centred on [Zn] = 0.2 M. **c** (i–vi) XFM tomography images at a 0° angle of an intact MII egg following zinc fixation. Zinc (i), sulfur (ii), copper (iv), iron (v) and calcium (vi) maps are shown with concentration ranges. The Zn/S map overlay (iii) demonstrates that zinc-rich regions are intracellular. **d**, Total metal content quantification in a resin-embedded MII egg following zinc fixation. Bars represent the average number of atoms over 60 projection images of the same sample (Fe = $8 \pm 4 \times 10^9$, Cu = $5 \pm 3 \times 10^9$, Zn = $6 \pm 2 \times 10^{10}$). Error bars represent \pm s.e.m. Dashed lines represent previously measured values in unfixed eggs⁵. The results indicate that this zinc-fixation protocol preserves the total zinc content. **e**, Zinc maps at several angles ($^\circ$) illustrate a cortical, hemispherical distribution of zinc-enriched regions.

total zinc concentrations within the vesicular stores. We found that these stores contained a zinc concentration range from ~ 0.05 to ~ 1.8 M per compartment, which was fitted to a median at [Zn] = 0.2 M (Fig. 4b).

X-ray fluorescence tomography demonstrates an asymmetric 3D distribution of cortical vesicles enriched in total zinc. To examine how these zinc-enriched vesicles are arranged in the 3D context of the MII egg, we mapped the elemental content of the MII egg using X-ray fluorescence tomography^{51,52}. In this approach, XFM maps of zinc-fixed and resin-embedded MII eggs were acquired at multiple rotation angles (Fig. 4c,e and Supplementary Movie 1), which provided an unprecedented 3D view of the total zinc distribution within an intact mammalian egg. The spatial distribution of total elemental zinc observed in the tomographic maps of the MII egg shows a number of similarities to that seen using vital fluorescent probes in the live egg. First, the XFM zinc map at the 0° rotation angle reveals a punctate distribution of sulfide-fixed zinc stores (Fig. 4c,i). These punctate zinc regions are localized within the cell as they overlay with the sulfur map, which highlights the total

volume of the egg (Fig. 4c,ii,iii). In addition, copper and iron maps (Fig. 4c,iv,v) do not exhibit a punctate pattern within the egg-cell proper, which suggests that zinc is the predominant metal contained within the cortical compartments. The zinc signal is also hemispherical, mirroring the labile zinc distribution revealed by live-cell fluorescence microscopy with ZincBY-1 (Fig. 4c,iv). This result is particularly striking as XFM directly measures X-ray photons emitted from zinc atoms, whereas ZincBY-1 fluorescence is a readout of the presence of labile Zn^{2+} ions. We found that the total number of zinc atoms measured within the embedded egg at all rotation angles yielded an average of $5.9 \pm 0.2 \times 10^{10}$ zinc atoms (Fig. 4d). This value is within 2% of previously quantified zinc data in non-embedded cells (5.8×10^{10} atoms⁵), which indicates that sulfide treatment preserves the native zinc content within the cell. Similarly, iron and copper contents are also preserved⁵. Additional zinc maps at different rotation angles (Fig. 4e) reveal that the punctate zinc signal is both hemispherical and cortical, which provides support for the conclusion that ZincBY-1 staining in live MII eggs corresponds to discrete subcellular sites that contain elevated levels of labile zinc relative to the cytosol.

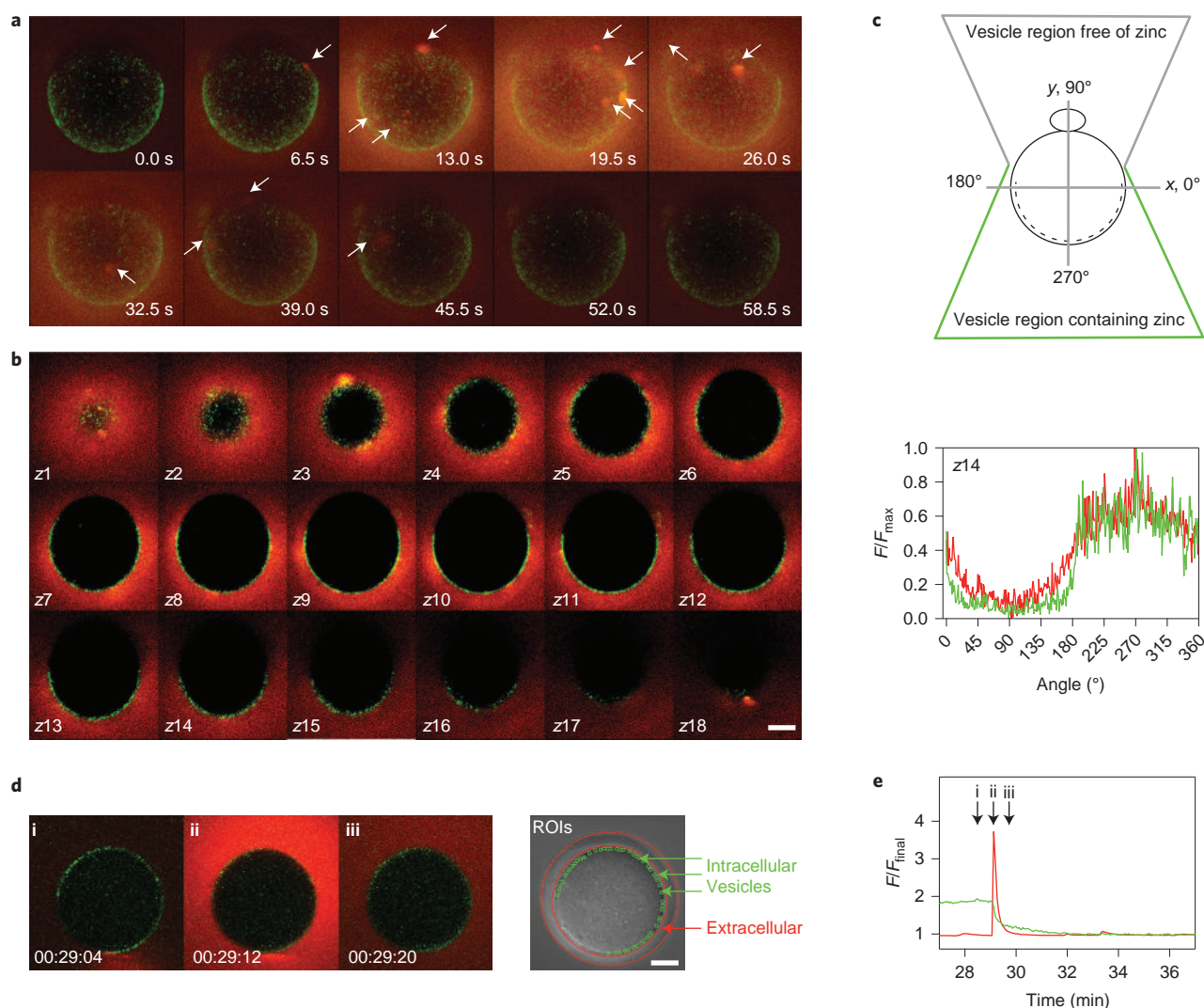


Figure 5 | Live-cell fluorescence zinc imaging demonstrates that intracellular zinc compartments are the source of the extracellular zinc spark. MII eggs labelled with 50 nM ZincBY-1 (intracellular, green) were activated with 10 mM SrCl_2 in a medium that contained 50 μM FluoZin-3 (extracellular, red). Scale bars, 20 μm . **a–c**, The whole egg was imaged in a z-stack time course (5 μm optical sections taken over 6.5 seconds). **a**, z-stack projections of ZincBY-1 and FluoZin-3 fluorescence during a zinc spark. The arrows indicate concentrated regions of zinc exocytosis. **b**, Overlaid optical sections of prespark ZincBY-1 fluorescence and FluoZin-3 fluorescence during a zinc spark. The z-stack position is indicated in each panel. **c**, Angular analysis of intracellular and extracellular fluorescence distribution in a z-section (z14 is shown, and the others are given in the Supplementary Information). The fluorescence intensity pattern is the same in both channels, which indicates that zinc-enriched vesicles are the source of the zinc spark. **d, e**, Egg imaged in a 1 μm confocal section. **d**, Images from a time course taken before (i), during (ii) and after (iii) a zinc spark. The brightfield image indicates intracellular and extracellular ROIs. **e**, Time traces show a simultaneous decrease in intracellular fluorescence and increase in extracellular fluorescence, which indicates that zinc-enriched vesicles are the source of the zinc spark.

Supplementary Video 1 shows the entire set of projections and a comparison between tomography and live-cell fluorescence imaging.

Compartmentalized zinc release on activation accounts for the zinc spark. Our previous studies demonstrated that labile zinc is lost from the egg via zinc sparks⁶. To determine whether zinc sparks arise from the coordinated release of zinc ions from the discrete cortical compartments described above, we analysed the spatiotemporal course of ZincBY-1-stained compartments concurrently with an extracellular zinc probe (FluoZin-3) at the time of egg activation. To analyse the zinc flux across the full surface of this large ($d = 70\text{--}75\ \mu\text{m}$) cell with the temporal resolution to capture a zinc-spark event (<10 seconds per frame), we acquired z-stacks with 5 μm thick optical sections during parthenogenetic egg activation (Fig. 5 and Supplementary Movie 2). In these time-course experiments, intracellular and

extracellular fluorescence emissions derive from ZincBY-1 and FluoZin-3, respectively. A 3D reconstruction of the optical sections (Fig. 5a and Supplementary Movie 2) revealed that zinc release into the medium occurs from multiple hot spots on the egg surface in the hemisphere that contains ZincBY-1-stained compartments. When the fluorescence intensities of intracellular zinc (prespark) and extracellular zinc (during spark) were plotted as a function of angle, we found a strong correlation (Fig. 5b,c). The regions with the highest intensities of extracellular fluorescence mapped to the hemisphere at the vegetal pole (270°), which is the same hemisphere that contained the highest intensity of intracellular fluorescence originating from zinc-rich vesicles. Similarly, the regions with the lowest zinc-spark intensities mapped to the zone free of zinc vesicles at the animal pole (90° , Fig. 5c and Supplementary Fig. 9). This geometric analysis strongly supports the hypothesis that the exocytosis of zinc-rich

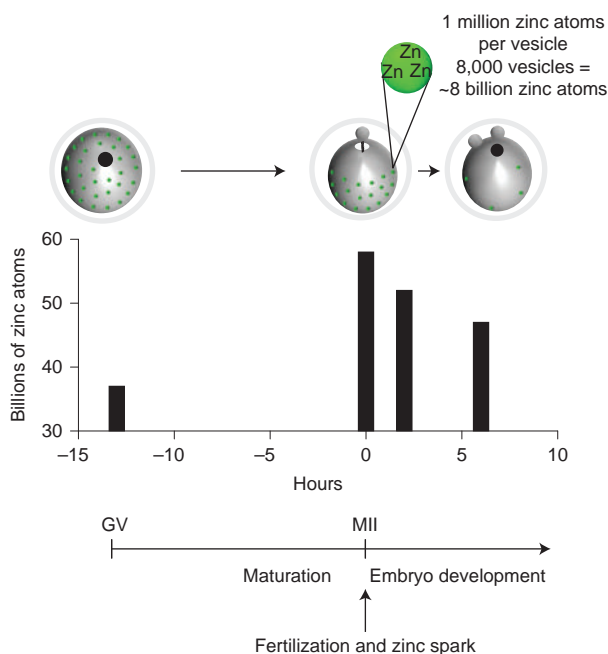


Figure 6 | The zinc flux during egg activation is regulated by a quantitative loss of cortical zinc compartments. This schematic diagram summarizes the fluxes in total zinc that are observed during maturation and immediately following fertilization/egg activation. The meiotic cycle in the mammalian egg occurs over a very short period of time and is accompanied by a very large flux in the amount and localization of the inorganic element zinc (black bars)^{5,6}. Through the combined use of our novel zinc probe, ZincBY-1, for live-cell imaging and a suite of fixed-cell imaging technologies (sulfide-zinc fixation, STEM-EDS, Bionanoprobe XFM, XFM tomography), we have estimated that there are 8,000 zinc-enriched cortical vesicles in the egg, each containing ~ 1 million zinc atoms. These vesicles, containing in total eight billion zinc atoms, are lost at fertilization during the zinc spark and quantitatively contribute to the zinc efflux that is required during the egg-to-embryo transition. This study sets a precedent for how zinc can be quantitatively tracked during key biological processes.

secretory compartments proximal to the ooplasmic membrane of the egg is the source of the extracellular zinc spark.

Although the z -resolution used to capture the zinc spark in 3D was too low to track individual vesicles, we performed subsequent higher-resolution imaging within a single optical section to enable vesicle tracking (Fig. 5d,e and Supplementary Movie 3). Prior to increases in extracellular fluorescence, ZincBY-1-labelled zinc-rich vesicles were visible at the cortex (Fig. 5d,i). Following the zinc spark (Fig. 5d,ii), the majority of compartmentalized cortical zinc staining was lost (Fig. 5d,iii). Normalized fluorescence time-traces demonstrated that the loss of punctate zinc staining occurs concurrently with the increase in extracellular fluorescence (Fig. 5e). This clearly shows that zinc-rich compartments are released by the cell during a zinc spark and are the source of exocytosed zinc. Some cortical staining remains after the zinc spark; this is not surprising as the egg releases between one and five sparks and thus will require additional vesicles for subsequent sparks to occur. These results are consistent with the observation that no bright cortical ZincBY-1 staining was observed in SrCl₂-activated parthenotes (Fig. 1c,vii,viii) relative to the GV oocyte (Fig. 1c,i,ii) and the MII egg (Fig. 1c,iv,v).

Discussion

Using complementary quantitative chemical approaches to map zinc at the single-cell level, we have defined a new family of discrete zinc-enriched vesicles that participate in the zinc fluxes that are essential in two critical stages of formation of a new mammal,

oocyte maturation and egg fertilization. Our development of a vital probe for labile zinc pools allows a qualitative interrogation of zinc fluxes at lower probe-incubation concentrations (that is, 50 nM) than commercially available and published agents. We used this intracellular probe along with extracellular FluoZin-3 to observe in concert the intracellular and extracellular components of the zinc spark⁶ as the coordinated exocytosis of thousands of zinc-enriched vesicles from the egg cortex. The identity of sites delineated by this probe as zinc-enriched vesicles was established using three different approaches that also allowed a more-extensive analysis of the zinc concentration in these compartments. Quantitative single-cell analysis revealed that this exocytosis is a mechanism underlying the previously discovered loss of zinc between the egg and early embryo stages^{5,6}. Specifically, fertilization or activation of the MII egg causes a steady loss of total zinc content—dropping by about 10% in the first two hours after fertilization and by 20% (that is, losing about 1×10^{10} zinc atoms) within the first six hours of fertilization. This lower zinc concentration then persists through the two-cell-embryo stage (Fig. 6). Given that vesicle-derived zinc sparks are produced by the egg within the first few hours of activation, we hypothesized that the 10–20% loss of total zinc content observed during this time period probably arose from the quantitative loss of zinc ions contained in cortical zinc vesicles. Precedence for this model comes from a variety of specialized cell types, including certain glutamatergic neurons^{19,20} and pancreatic β -islet cells^{18,22}, in which the zinc efflux is associated with zinc-rich secretory vesicles. However, studies of zinc compartments within these systems have been largely qualitative.

By applying a suite of single-cell quantitative analytical methods, we can account for this zinc flux during mammalian fertilization. Quantitative characterization of zinc-rich compartments allows a mass balance calculation of changes in the zinc compartmentalization at the time of egg activation. Based on the absolute vesicular zinc content, we can gauge the percentage of total cellular zinc that is in the cortical compartments (Supplementary Fig. 10 and Supplementary Table 3). We measured an average total zinc concentration of 0.2 M within a vesicle (Bionanoprobe XFM). Previous studies in hippocampal systems estimated a 300 μ M concentration for labile zinc within secretory vesicles in mossy fibre boutons⁵³. The concentrations we determined in the context of the egg are orders of magnitude higher than those previously measured in other systems (Fig. 4b). The 0.2 M value reported here for the mouse-egg vesicles may have contributions from both labile and tightly bound zinc ions. Using an average radius of 130 nm per vesicle (obtained from STEM measurements, Fig. 3d) and the 0.2 M average zinc concentration per vesicle, we estimate that an individual compartment contains about 1×10^6 zinc atoms. Given a total of approximately 8,000 cortical zinc-rich compartments in the MII egg (live-cell fluorescence microscopy, Fig. 1c), we estimate that the sum total of zinc in all cortical compartments corresponds to about 8×10^9 zinc atoms, or $\sim 15\%$ of the total zinc content of an MII egg (Fig. 6; further calculation details and error analysis are provided in the Supplementary Information, Supplementary Fig. 10 and Supplementary Table 3). This number lies well within the 10–20% loss of total zinc observed in the hours following fertilization, as reported in the literature^{5,6}. Taken together, the similarity between the number of compartmentalized zinc atoms (8×10^9) and the number of zinc atoms lost following fertilization (1×10^{10}) indicates that cortical zinc compartments in the egg drive the zinc decreases that are requisite during fertilization. These results demonstrate that the egg sequesters zinc at high concentrations in vesicles at the cortex and subsequently releases the content of these compartments at the time of egg activation.

These cortical zinc-rich vesicles released during egg activation have a number of potential functions during fertilization. The changes in distribution and quantity of these vesicles throughout

maturation and activation mirror those of CGs. These secretory vesicles are released at fertilization and contain biochemical species, including enzymes, that modify the egg's ZP and thus play a role in the block to polyspermy^{41,42}. Intriguingly, one of the known CG proteins, the zinc metalloprotease ovastacin, has been shown to cleave the ZP glycoprotein ZP2 in a key step of zona hardening and prevention of polyspermy⁴³. Alternatively, zinc released by the egg could act directly on sperm to alter their function given the importance of zinc in mammalian sperm physiology^{34,35,54,55}. Thus metals released during the zinc spark and the cortical reaction may play a number of roles outside the cell.

This study lays the groundwork for understanding how zinc fluxes can regulate events in multiple biological systems beyond the egg. At fertilization, the egg exploits a precise machinery for lowering intracellular zinc, that is, the coordinated exocytosis of zinc-rich vesicles. Having quantitatively identified a major zinc-regulation pathway in the egg during fertilization, we now stand poised to understand how zinc partitions between permissive and instructive functions in the biology of cellular transitions during development and beyond.

Methods

Here we describe key experiments—an extended experimental section is provided in the Supplementary Methods.

Synthesis of ZincBY-1. 3-Chloro-5-methoxy-8-mesityl-BODIPY (**1**) (32 mg, 0.085 mmol) and *N,N,N'*-tris(pyridin-2-ylmethyl)ethane-1,2-diamine (**2**) (57 mg, 0.17 mmol) were combined in 5 ml dry CH₃CN in an oven-dried Schlenk flask under N₂. The reaction was heated at 80 °C overnight. After cooling and solvent removal, the product was purified by silica gel chromatography (0–5% CH₃OH in CH₂Cl₂) to yield the pure product as a dark pink residue (40 mg, 70% yield). ¹H NMR (CDCl₃, 500 MHz): δ 8.51 (1H, m), 8.48 (2H, m), 7.62 (3H, dq, *J* = 2.0, 7.5 Hz), 7.53 (2H, d, *J* = 8.0 Hz), 7.37 (1H, d, *J* = 8.0 Hz), 7.15 (1H, m), 7.12 (2H, m), 6.89 (2H, s), 6.34 (1H, d, *J* = 4.5), 6.10 (1H, d, *J* = 4.0 Hz), 5.87 (1H, d, *J* = 4.5 Hz), 5.61 (1H, d, *J* = 4.0 Hz), 5.22 (2H, s), 3.96 (3H, s), 3.89 (4H, s), 3.86 (2H, m), 2.92 (2H, m), 2.33 (3H, s), 2.08 (6H, s). High-resolution electrospray ionization mass spectrometry MH⁺, C₃₉H₄₁BF₂N₇O⁺ calc. 672.3428, found 672.3432. NMR spectra were obtained on a Bruker Avance-III 500 MHz. The high-resolution mass spectra were measured on an Agilent 6210 LC-TOF. Additional experimental details are provided in the Supplementary Methods.

Animals, cell collection and culture. GV-stage oocytes were isolated from cumulus–oocyte complexes (COCs) collected from the ovaries of sexually mature (6–10 weeks) female CD-1 mice injected with 5 IU pregnant mare's serum gonadotropin (PMSG, Sigma-Aldrich) 48 hours before sample collection. Collection was performed in Leibovitz's L-15 medium (Life Technologies) supplemented with 1% (v/v) fetal bovine serum (Life Technologies) and 0.2 mM 3-isobutyl-1-methylxanthine (Sigma-Aldrich). To collect MII-arrested eggs at the MII stage, females were injected with 5 IU PMSG and then 5 IU human chorionic gonadotropin (hCG, Sigma-Aldrich) 46 hours later. Eggs were isolated from the oviducts 14 hours after the administration of hCG. Cumulus cells were denuded using 0.3% (w/v) hyaluronidase. Parthenotes were obtained by activating MII eggs in 10 mM SrCl₂ in calcium-free potassium simplex-optimized medium (KSOM) (Millipore) for three hours at 37 °C in an atmosphere of 5% CO₂. Successfully activated cells were selected based on extrusion of the second polar body. Animals were treated in accordance with the US National Institutes of Health Guide for the Care and Use of Laboratory Animals. Food and water were given *ad libitum*. The Northwestern University Institutional Animal Care and Use Committee approved all the protocols.

Live-cell confocal microscopy. Confocal microscopy was performed on a Leica SP5 resonant scanner confocal microscope (Biological Imaging Facility, Northwestern University) and a Zeiss LSM 510 Confocal Microscope (Quantitative Bioelemental Imaging Center, Northwestern University). Intracellular zinc was visualized using 50 nM ZincBY-1 and extracellular zinc was visualized using 50 μM FluoZin-3 (Life Technologies). DNA was visualized using 10 μg ml⁻¹ Hoechst 33342. In the figures, fluorescence images within the same panel were collected and displayed using the same parameters. In the activation experiments, eggs were activated using 10 mM SrCl₂ in calcium-free KSOM (Millipore). Further experimental details are provided in the Supplementary Methods.

Zinc-fixation of MII eggs. Following the collection of MII eggs, the cells were fixed in 4% paraformaldehyde in PBS for one hour in the fridge. After fixation, the eggs were transferred into methyl cellulose capillaries and then transferred to solutions of NaHS in PBS (pH 7) at 4 °C or, for the controls, in PBS only. NaHS solutions were prepared by dissolving Na₂S in PBS over ice and adjusting the

solution pH to 7 using concentrated HNO₃ immediately prior to use. After 30 minutes of NaHS treatment, the eggs in the capillaries were dehydrated in 10%, 25%, 50%, 75%, 90% and 2 × 100% ethanol for 15 minutes each on ice. The samples were infiltrated with a 1:1 mixture of Spurr resin (Electron Microscopy Sciences (EMS)) and ethanol for two hours, followed by pure Spurr resin overnight at 4 °C. The next day, the samples were placed in fresh Spurr resin in flat embedding moulds and polymerized for 72 hours at 65 °C. Ultrathin sections were obtained with a diamond knife (Diatome) in an ultramicrotome (UC7, Leica).

STEM-EDS. Ultrathin sections of 200 nm nominal thickness were placed on molybdenum slot grids with a carbon-coated Formvar support film (EMS) and observed unstained. The sections were observed and analysed with a dual EDS system in a Hitachi STEM HD2300A at a 200 kV acceleration voltage, using a 75 μm objective aperture and 691 pA probe current. The electron dose was about 8.77 × 10³ electrons per square nanometre (per single frame, 45 frames were recorded) in the spectral imaging mode for elemental maps. Elemental ratios in ZnS crystals were determined by removing the background with a digital top-hat filter and by using the Cliff–Lorimer matrix correction without absorption. All EDS data analyses were carried out with the NSS Noran System Seven 2.2 Software (Thermo Scientific). Image resolution was determined based on the dimensions of the smallest recognizable areas in the elemental maps that contain pixels with a zinc-specific signal.

Received 1 July 2014; accepted 11 November 2014;
published online 15 December 2014; corrected online
23 December 2014

References

- Berg, J. M. & Shi, Y. The galvanization of biology: a growing appreciation for the roles of zinc. *Science* **271**, 1081–1085 (1996).
- Finney, L. A. & O'Halloran, T. V. Transition metal speciation in the cell: insights from the chemistry of metal ion receptors. *Science* **300**, 931–936 (2003).
- O'Halloran, T. V. Transition metals in control of gene expression. *Science* **261**, 715–725 (1993).
- Maret, W. Zinc biochemistry: from a single zinc enzyme to a key element of life. *Adv. Nutr.* **4**, 82–91 (2013).
- Kim, A. M., Vogt, S., O'Halloran, T. V. & Woodruff, T. K. Zinc availability regulates exit from meiosis in maturing mammalian oocytes. *Nature Chem. Biol.* **6**, 674–681 (2010).
- Kim, A. M. *et al.* Zinc sparks are triggered by fertilization and facilitate cell cycle resumption in mammalian eggs. *ACS Chem. Biol.* **6**, 716–723 (2011).
- Bernhardt, M. L., Kim, A. M., O'Halloran, T. V. & Woodruff, T. K. Zinc requirement during meiosis I–meiosis II transition in mouse oocytes is independent of the MOS–MAPK pathway. *Biol. Reprod.* **84**, 526–536 (2011).
- Bernhardt, M. L., Kong, B. Y., Kim, A. M., O'Halloran, T. V. & Woodruff, T. K. A zinc-dependent mechanism regulates meiotic progression in mammalian oocytes. *Biol. Reprod.* **86**, 114 (2012).
- Kong, B. Y., Bernhardt, M. L., Kim, A. M., O'Halloran, T. V. & Woodruff, T. K. Zinc maintains prophase I arrest in mouse oocytes through regulation of the MOS–MAPK pathway. *Biol. Reprod.* **87**, 11, 11–12 (2012).
- Suzuki, T., Yoshida, N., Suzuki, E., Okuda, E. & Perry, A. C. Full-term mouse development by abolishing Zn²⁺-dependent metaphase II arrest without Ca²⁺ release. *Development* **137**, 2659–2669 (2010).
- Tian, X. & Diaz, F. J. Zinc depletion causes multiple defects in ovarian function during the periovulatory period in mice. *Endocrinology* **153**, 873–886 (2012).
- Krauchunas, A. R. & Wolfner, M. F. In *Gametogenesis* (ed. Wassarman P. M.) 267–292 (Current Topics in Developmental Biology, 102, Academic Press, 2013).
- Suzuki, T. *et al.* Mouse Emi2 as a distinctive regulatory hub in second meiotic metaphase. *Development* **137**, 3281–3291 (2010).
- Kong, B. Y. *et al.* Maternally-derived zinc transporters ZIP6 and ZIP10 drive the mammalian oocyte-to-egg transition. *Mol. Hum. Reprod.* **20**, 1077–1089 (2014).
- Catterall, A. Structure and function of voltage-gated ion channels. *Annu. Rev. Biochem.* **64**, 493–531 (1995).
- Cousins, R. J., Liuzzi, J. P. & Lichten, L. A. Mammalian zinc transport, trafficking, and signals. *J. Biol. Chem.* **281**, 24085–24089 (2006).
- Kühlbrandt, W. Biology, structure and mechanism of P-type ATPases. *Nature Rev. Mol. Cell Biol.* **5**, 282–295 (2004).
- Chimienti, F., Devergnas, S., Favier, A. & Seve, M. Identification and cloning of a beta-cell-specific zinc transporter, ZnT-8, localized into insulin secretory granules. *Diabetes* **53**, 2330–2337 (2004).
- Frederickson, C. J., Suh, S. W., Silva, D., Frederickson, C. J. & Thompson, R. B. Importance of zinc in the central nervous system: the zinc-containing neuron. *J. Nutr.* **130**, 1471S–1483S (2000).
- Palmiter, R. D., Cole, T. B., Quaife, C. J. & Findley, S. D. ZnT-3, a putative transporter of zinc into synaptic vesicles. *Proc. Natl Acad. Sci. USA* **93**, 14934–14939 (1996).
- Yamasaki, S. *et al.* Zinc is a novel intracellular second messenger. *J. Cell Biol.* **177**, 637–645 (2007).

22. Zalewski, P. D. *et al.* Video image analysis of labile zinc in viable pancreatic islet cells using a specific fluorescent probe for zinc. *J. Histochem. Cytochem.* **42**, 779–884 (1994).
23. Fierke, C. A. & Thompson, R. B. Fluorescence-based biosensing of zinc using carbonic anhydrase. *Biomaterials* **14**, 205–222 (2001).
24. Palmer, A. E., Qin, Y., Park, J. G. & McCombs, J. E. Design and application of genetically encoded biosensors. *Trends Biotechnol.* **29**, 144–152 (2011).
25. Que, E. L., Domaille, D. W. & Chang, C. J. Metals in neurobiology: probing their chemistry and biology with molecular imaging. *Chem. Rev.* **108**, 1517–1549 (2008).
26. Tomat, E. & Lippard, S. J. Imaging mobile zinc in biology. *Curr. Opin. Chem. Biol.* **14**, 225–230 (2010).
27. Fahrni, C. J. & O'Halloran, T. V. Aqueous coordination chemistry of quinoline-based fluorescence probes for the biological chemistry of zinc. *J. Am. Chem. Soc.* **121**, 11448–11458 (1999).
28. Cork, R. Problems with the application of quin-2-AM to measuring cytoplasmic free calcium in plant cells. *Plant Cell Environ.* **9**, 157–161 (1986).
29. Laha, J. K., Dhanalekshmi, S., Taniguchi, M., Ambrose, A. & Lindsey, J. S. A Scalable synthesis of meso-substituted dipyrromethanes. *Org. Proc. Res. Devel.* **7**, 799–812 (2003).
30. Domaille, D. W., Zeng, L. & Chang, C. J. Visualizing ascorbate-triggered release of labile copper within living cells using a ratiometric fluorescent sensor. *J. Am. Chem. Soc.* **132**, 1194–1195 (2010).
31. Hureau, C. *et al.* Syntheses, X-ray structures, solid state high-field electron paramagnetic resonance, and density-functional theory investigations on chloro and aqua Mn^{II} mononuclear complexes with amino-pyridine pentadentate ligands. *Inorg. Chem.* **47**, 9238–9247 (2008).
32. Ambundo, E. A. *et al.* Influence of coordination geometry upon copper(II/I) redox potentials. Physical parameters for twelve copper tripodal ligand complexes. *Inorg. Chem.* **38**, 4233–4242 (1999).
33. Rae, T. D., Schmidt, P. J., Pufahl, R. A., Culotta, V. C. & O'Halloran, T. V. Undetectable intracellular free copper: the requirement of a copper chaperone for superoxide dismutase. *Science* **284**, 805–808 (1999).
34. Andrews, J. C., Nolan, J. P., Hammerstedt, R. H. & Bavister, B. D. Role of zinc during hamster sperm capacitation. *Biol. Reprod.* **51**, 1238–1247 (1994).
35. Stoltenberg, M. *et al.* Autometallographic demonstration of zinc ions in rat sperm cells. *Mol. Hum. Reprod.* **3**, 763–767 (1997).
36. Zalewski, P. *et al.* Use of a zinc fluorophore to measure labile pools of zinc in body fluids and cell-conditioned media. *Biotechniques* **40**, 509–520 (2006).
37. Outten, C. E. & O'Halloran, T. V. Femtomolar sensitivity of metalloregulatory proteins controlling zinc homeostasis. *Science* **292**, 2488–2492 (2001).
38. Fahrni, C. J. Synthetic fluorescent probes for monovalent copper. *Curr. Opin. Chem. Biol.* (2013).
39. Gee, K. R., Zhou, Z. L., Qian, W. J. & Kennedy, R. Detection and imaging of zinc secretion from pancreatic beta-cells using a new fluorescent zinc indicator. *J. Am. Chem. Soc.* **124**, 776–778 (2002).
40. Burdette, S. C., Frederickson, C. J., Bu, W. & Lippard, S. J. ZP4, an improved neuronal Zn²⁺ sensor of the Zinpyr family. *J. Am. Chem. Soc.* **125**, 1778–1787 (2003).
41. Ducibella, T., Anderson, E., Albertini, D. F., Aalberg, J. & Rangarajan, S. Quantitative studies of changes in cortical granule number and distribution in the mouse oocyte during meiotic maturation. *Dev. Biol.* **130**, 184–197 (1988).
42. Wessel, G. M. *et al.* The biology of cortical granules. *Int. Rev. Cytol.* **209**, 117–206 (2001).
43. Burkart, A. D., Xiong, B., Baibakov, B., Jimenez-Movilla, M. & Dean, J. Ovastacin, a cortical granule protease, cleaves ZP2 in the zona pellucida to prevent polyspermy. *J. Cell Biol.* **197**, 37–44 (2012).
44. Tahara, M. *et al.* Dynamics of cortical granule exocytosis at fertilization in living mouse eggs. *Am. J. Physiol.* **270**, C1354–1361 (1996).
45. Stika, K. M., Bielat, K. L. & Morrison, G. H. Diffusible ion localization by ion microscopy: a comparison of chemically prepared and fast-frozen, freeze-dried, unfixed liver sections. *J. Microsc.* **118**, 409–420 (1980).
46. Timm, F. Histochemistry of heavy metals; the sulfide-silver procedure. *Dtsch. Z. Gesamte Gerichtl. Med.* **46**, 706–711 (1958).
47. Danscher, G., Stoltenberg, M., Bruhn, M., Sondergaard, C. & Jensen, D. Immersion autometallography: histochemical *in situ* capturing of zinc ions in catalytic zinc-sulfur nanocrystals. *J. Histochem. Cytochem.* **52**, 1619–1625 (2004).
48. Licht, S. Aqueous solubilities, solubility products and standard oxidation-reduction potentials of the metal sulfides. *J. Electrochem. Soc.* **135**, 2971–2975 (1988).
49. Wu, J. S. *et al.* Imaging and elemental mapping of biological specimens with a dual-EDS dedicated scanning transmission electron microscope. *Ultramicroscopy* **128**, 24–31 (2013).
50. Chen, S. *et al.* The Bionanoprobe: hard X-ray fluorescence nanoprobe with cryogenic capabilities. *J. Synchrotron Radiat.* **21**, 66–75 (2014).
51. Hong, Y. P. *et al.* Alignment of low-dose X-ray fluorescence tomography images using differential phase contrast. *J. Synchrotron Radiat.* **21**, 229–234 (2014).
52. Gleber, S.-C. *et al.* New developments in hard X-ray fluorescence microscopy for *in-situ* investigations of trace element distributions in aqueous systems of soil colloids. *J. Phys. Conf. Ser.* **463**, 012005 (2013).
53. Frederickson, C. J., Klitenick, M. A., Manton, W. I. & Kirkpatrick, J. B. Cytoarchitectonic distribution of zinc in the hippocampus of man and the rat. *Brain Res.* **273**, 335–339 (1983).
54. Foresta, C. *et al.* Role of zinc trafficking in male fertility: from germ to sperm. *Hum. Reprod.* **29**, 1134–1145 (2014).
55. Lishko, P. V. & Kirichok, Y. The role of Hv1 and CatSper channels in sperm activation. *J. Physiol.* **588**, 4667–4672 (2010).

Acknowledgements

The authors thank members of the O'Halloran, Woodruff and Dravid labs for scientific discussions and advice. We thank E. W. Roth for the preparation of electron microscopy samples and J.-H. Chung and J. Shangguan for help with chemical syntheses. Equipment and experimental guidance were provided by the following core facilities at Northwestern University: the Integrated Molecular Structure Education and Research Center, the Biological Imaging Facility, the Quantitative Bioelemental Imaging Center, the Electron Probe Instrumentation Centre and the Keck Biophysics Facility. This research used resources of the Advanced Photon Source, a US Department of Energy (DOE) Office of Science User Facility operated for the DOE Office of Science by Argonne National Laboratory under contract no. DE-AC02-06CH11357. This work was supported by a Medical Research Award from the W. M. Keck Foundation, a SPARK Award from the Chicago Biomedical Consortium and the National Institutes of Health (P01 HD021921, GM38784, U54HD076188 and T32GM105538).

Author contributions

E.L.Q., R.B., F.E.D., B.Y.K., V.P.D., T.K.W. and T.V.O. designed the research. E.L.Q., R.B., F.E.D., B.Y.K., S.A.G. and A.R.B. performed the research. S.C.G., S.V. and S.C. helped design and implement XFM experiments and process and analyse the data. E.L.Q., R.B., F.E.D., T.K.W. and T.V.O. wrote the manuscript. All the authors discussed the results and commented on the manuscript.

Additional information

Supplementary information is available in the [online version](#) of the paper. Reprints and permissions information is available online at www.nature.com/reprints. Correspondence and requests for materials should be addressed to T.K.W. and T.V.O.

Competing financial interests

The authors declare no competing financial interests.